Check for updates

MOF-derived NiAl$_2$O$_4$/NiCo$_2$O$_4$ porous materials as supercapacitors with high electrochemical performance

Changyu Hu,[a] Huidong Xie, (iD) *[a] Yibo Wang,[a] Hu Liu,[a] Yajuan Zhao[a] and Chang Yang[b]

Metal–organic framework compounds are extensively utilized in various fields, such as electrode materials, owing to their distinctive porous structure and significant specific surface area. In this study, NiCoAl-MOF metal–organic framework precursors were synthesized by a solvothermal method, and NiAl$_2$O$_4$/NiCo$_2$O$_4$ electrode materials were prepared by the subsequent calcination of the precursor. These materials were characterized by XRD, XPS, BET tests, and SEM, and the electrochemical properties of the electrode materials were tested by CV and GCD methods. BET tests showed that NiAl$_2$O$_4$/NiCo$_2$O$_4$ has an abundant porous structure and a large specific surface area of up to 105 m^2 g^{-1}. The specific capacitance of NiAl$_2$O$_4$/NiCo$_2$O$_4$ measured by the GCD method reaches up to 2870.83 F g^{-1} at a current density of 1 A g^{-1}. The asymmetric supercapacitor NiAl$_2$O$_4$/NiCo$_2$O$_4$//AC assembled with activated carbon electrodes has a maximum energy density of 166.98 W h kg^{-1} and a power density of 750.00 W kg^{-1} within a voltage window of 1.5 V. In addition, NiAl$_2$O$_4$/NiCo$_2$O$_4$ materials have good cycling stability. These advantages make it a good candidate for the application of high-performance supercapacitors.

1. Introduction

Currently, environmental pollution, a fossil energy crisis, global warming, and other issues have deeply stimulated research on new environmentally friendly energy storage technologies. Efficient energy storage technology is the key to the development of new energy sources, which can solve the contradiction of energy supply and demand imbalance by energy conversion of different types of energies.[1–3] With the increasing use of movable electronic devices and new energy vehicles, there are high requirements for the energy storage performance of the devices. Supercapacitors are considered as the most promising energy storage devices due to their high power density, short charging time, and long cycle life. Pseudocapacitor materials can store charges based on a rapid and reversible electrochemical redox reaction that occurs during the charge and discharge process. Because the charge storage is carried out by electron transfer between different valence states of a chemical element, pseudocapacitors have the advantages of high specific capacity and power density.[4]

Metal–organic framework (MOF) compounds have been widely used as electrode materials because of their unique morphological structure and good electrical conductivity.[5,6] MOF materials can be used as ideal precursors for preparing porous active substances in supercapacitors and other energy storage devices.[7–9] The significantly high surface area of porous structures helps to increase the effective contact between the electrode material and the electrolyte, improving the charge storage capacity. At the same time, the channels and pores of porous structures optimize the transport rate of ions or molecules through the electrode material, reducing resistive losses and thus improving energy conversion efficiency. MOF-derived metal oxides can be adjusted in terms of specific surface areas and pore size distributions by changing annealing temperature and time. Among them, metal oxides derived from Ni and Co-based MOF materials, which have high theoretical specific capacitance and stable electrochemical properties, are inexpensive, environmentally friendly, and widely reported. Liu *et al.* incorporated both Cu dopants and O vacancies into Co$_3$O$_4$ nanocrystals confined in a carbon matrix (Ov–Cu–Co$_3$O$_4$@C), which showed a high energy density of 64.1 W h kg^{-1} at 800 W kg^{-1}. Meanwhile, asymmetric supercapacitors exhibited good flexibility with no significant performance degradation at different bending states.[10–12] Zeng *et al.*[13] prepared self-assembled yolk–shell hierarchical microstructured bimetallic metal framework materials (NiZn-MOFs) using a simple solvohydrothermal

[a] *School of Chemistry and Chemical Engineering, Xi'an University of Architecture and Technology, Xi'an, 710055, Shaanxi, China.*
 E-mail: xiehuidong@tsinghua.org.cn; Tel: 00-86-29-82203378
[b] *Engineering Comprehensive Training Center, Xi'an University of Architecture and Technology, Xi'an, 710055, Shaanxi, China*

6616 | *Phys. Chem. Chem. Phys.*, 2024, **26**, 6616–6626

This journal is © the Owner Societies 2024

method. The as-prepared sample showed a specific capacitance of 88.66 F g^{-1} at a current density of 1.1 A g^{-1} and a capacity retention of 90.05% after 2000 cycles at a current density of 8 A g^{-1}. Abbas *et al.*[14] synthesized a novel Cu-MOF by a simple method and prepared MOF-derived multilevel hierarchy Cu/Cu$_{x}$-O@NC materials after annealing for 4 h. In a three-electrode system, the MOF-derived sample achieved a specific capacitance of 547 F g^{-1} at 1 A g^{-1} and a cyclic retention of 91.81% after 10 000 GCD cycles. Salehi *et al.*[15] used one-step reduction electrochemistry to grow bimetal-terephthalate (CoZn-MOF) materials on nickel foam, which exhibited a specific capacitance of 1205 F g^{-1} and a capacity retention of 94.8% after 8000 cycles at a current density of 2 A g^{-1}. Abbas *et al.* presented a novel "one-step" liquid phase co-exfoliation method for producing high-quality co-exfoliated graphene nanoplatelets (GNP)/MoS$_2$. The hybrid materials demonstrated a superior supercapacitor performance with a specific capacitance of 311.14 F g^{-1} at 1 A g^{-1} and an excellent cycling stability (98.35% over 2000 cycles). They can be further applied in an asymmetric supercapacitor device powering a commercial LED up to 90 seconds.[16–18]

Despite the good cycling performance of the MOF-derived materials mentioned above, the relatively low specific capacitance limits the practical application.[19] Spinel aluminates have good thermal and chemical stabilities, but poor electrical conductivity, which can be improved by introducing metals with good electrical conductivity such as Co and Ni. MOF-derived Al oxides have a stable structure that prevents the transition metal from dissolving into the electrolyte.

In this experiment, Co/Ni/Al-MOF precursors were prepared by a solvothermal method, and then MOF-derived metal oxides, NiAl$_2$O$_4$/NiCo$_2$O$_4$, with porous structures were prepared by calcining the precursors. The electrochemical properties of the materials and asymmetric supercapacitors were tested, including cyclic voltammetry (CV), galvanostatic charge–discharge (GCD), and electrochemical impedance spectra (EIS). Meanwhile, an asymmetric supercapacitor (ASC) was assembled with activated carbon (AC) as the anode and NiAl$_2$O$_4$/NiCo$_2$O$_4$ as the cathode.

2. Experimental

2.1 Preparation of NiAl$_2$O$_4$/NiCo$_2$O$_4$

The reagents used were analytically pure and did not require further purification for use. First, 10 mL of *N*,*N*-dimethylformamide (DMF), 10 mL of anhydrous ethanol, and 10 mL of deionized water were mixed to form a transparent solution. Then, 0.75 g of Co(NO$_3$)$_2$·6H$_2$O, 0.75 g of Ni(NO$_3$)$_2$·6H$_2$O, 0.54 g of 1,3,5-benzene tricarboxylic acid, and 0.97 g of Al(NO$_3$)$_3$·9H$_2$O (molar ratio = 1:1:1:1) were added to the above-mixed solution with stirring. After dissolving completely, the solution was transferred to an autoclave of 50 mL and allowed to react at 105 °C for 20 h. Next, the autoclave was cooled to room temperature, and the product was centrifuged and washed three times with anhydrous ethanol. The powder of Co/Ni/Al-MOF was obtained by drying the product at 110 °C for 12 h. The dried product was ground using a mortar and then calcined

under a N$_2$ atmosphere at 550 °C for 30 min. Finally, the calcined samples were annealed in air at 350 °C for 120 min and denoted as NiAl$_2$O$_4$/NiCo$_2$O$_4$. For comparison, single metallic and bimetallic materials were prepared under a similar condition and denoted as Ni, Ni/Al, and Co/Al.

2.2. Electrochemical measurements

The working electrodes were coated on nickel foam (working area of 1×1 cm^2) with a slurry of active substances, Cochin black, and PVDF in a mass ratio of 8:1:1. The electrochemical properties were tested using a three-electrode system, with HgO/Hg electrode and Pt electrode as the reference and counter electrodes, respectively. Electrochemical tests were performed in the 6 M KOH electrolyte using a CHI660E electrochemical workstation. The electrochemical properties of the samples were tested by cyclic voltammetry (CV), galvanostatic charge–discharge (GCD) analysis, and electrochemical impedance spectroscopy (EIS).

2.3. Material characterization

X-ray diffraction (XRD) patterns were measured using a Bruker D8 Advance diffractometer (Germany) with Cu-Kα radiation ($\lambda = 1.5418$ Å) accelerated at 40 kV in the 2θ range of 10–80°. X-ray photoelectron spectra (XPS) were recorded with a Thermo Scientific K-Alpha instrument in the USA. The morphology of the products was observed using a GeminiSEM500 field emission scanning electron microscope (SEM). The N$_2$ adsorption/desorption isotherms were performed using a Quantachrome Autosorb IQ3 chemisorber.

3. Results and discussion

3.1. Characterization

To check the composition of the material, XRD analysis was performed and the result is shown in Fig. 1. Peaks at 18.94, 31.18, 36.74, 44.67, and 65.03° are attributed to the (111) (220) (311) (400) (440) crystal planes of CoAl$_2$O$_4$ (JCPDS: 82-2250).
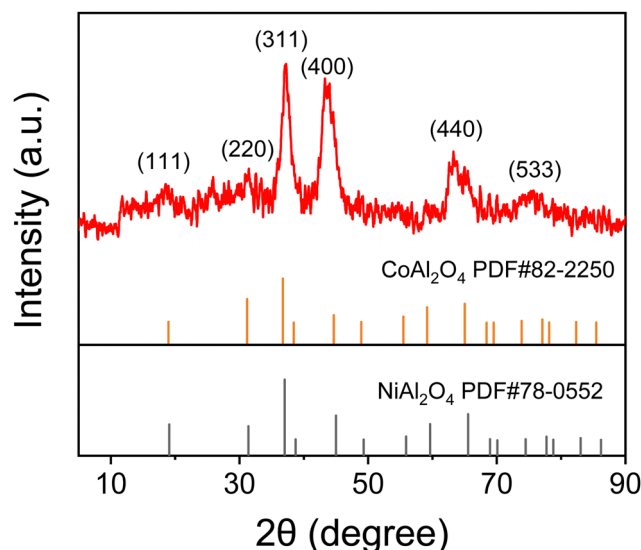

Fig. 1 XRD pattern of NiAl$_2$O$_4$/NiCo$_2$O$_4$.

This journal is © the Owner Societies 2024

Phys. Chem. Chem. Phys., 2024, **26**, 6616–6626 | **6617**

Peaks at 19.08, 31.41, 37.01, 45.01 and 65.54° correspond to the (111) (220) (311) (400) (440) crystal planes of $NiAl_2O_4$ (JCPDS: 78-0552). It is well known that MOF peaks are generally present at low angles. Since there are no diffraction peaks in the range of 5–10°, XRD shows that the MOFs have been converted to oxides. During the annealing process, the MOF structure partially collapsed and the organic ligands underwent carbonization and decomposition. Meanwhile, the low peak intensity indicates a low crystallinity of the material. It has been reported that low crystallinity is beneficial for providing short transport paths for ions in the electrolyte within the electrode material, which is conducive to improving the electrochemical performance.[20]

Fig. 2 shows the high-resolution and survey XPS spectra of $NiAl_2O_4/NiCo_2O_4$. The Al 2p spectra in Fig. 2a can be fitted into two peaks and the Al $2p_{3/2}$ binding energy of 73.9 eV agrees with Al^{3+}.[21] The C 1s spectra can be fitted into three peaks at 284.8, 286.2, and 288.9 eV, corresponding to the C–C, C–O–C, and O–C=O bonds in the MOF structure, respectively,[22] as illustrated in Fig. 2b. From Fig. 2c, two main peaks at 780.1 eV (Co $2p_{3/2}$) and 796.4 eV (Co $2p_{1/2}$) agree with the presence of Co^{3+} in $NiCo_2O_4$. Meanwhile, two peaks at 787.1 and 803.7 eV can be

attributed to the satellite peaks.[23,24] Two peaks in Fig. 2d at 855.4 eV and 873.1 eV correspond to Ni^{2+}, and two satellite peaks at 861.4 and 879.1 eV are also found.[25] In Fig. 2e, the fitted O 1s peaks at 532.2, 531.1 and 529.7 eV can be attributed to adsorbed oxygen, TM–O (TM = Co, Ni), and lattice oxygen, respectively.[26] The presence of C 1s, Ni 2p, Co 2p, Al 2p, and O 1s can be identified well from Fig. 2f, which proves the successful preparation of the $NiAl_2O_4/NiCo_2O_4$ composites.

Fig. 3 shows the nitrogen adsorption–desorption isotherm and pore size distribution of $NiAl_2O_4/NiCo_2O_4$ and MOFs. From Fig. 3a, the adsorption–desorption curve has a typical type IV curve with an H3-type hysteresis loop, which is usually present in solids containing agglomerated particles that form fissure-like pores of heterogeneous size and shape. In addition, the isotherm has no obvious saturation adsorption plateau, indicating that the pore structure is very irregular.[27] A specific surface area of 105 m^2 g^{-1} is obtained using the Brunauer–Emmett–Teller (BET) model, indicating that the $NiAl_2O_4/NiCo_2O_4$ material has the property of the mesoporous structure. Fig. 3b shows that the pore size distribution is scattered between 2 and 50 nm, with a few large pores at 50–82 nm.
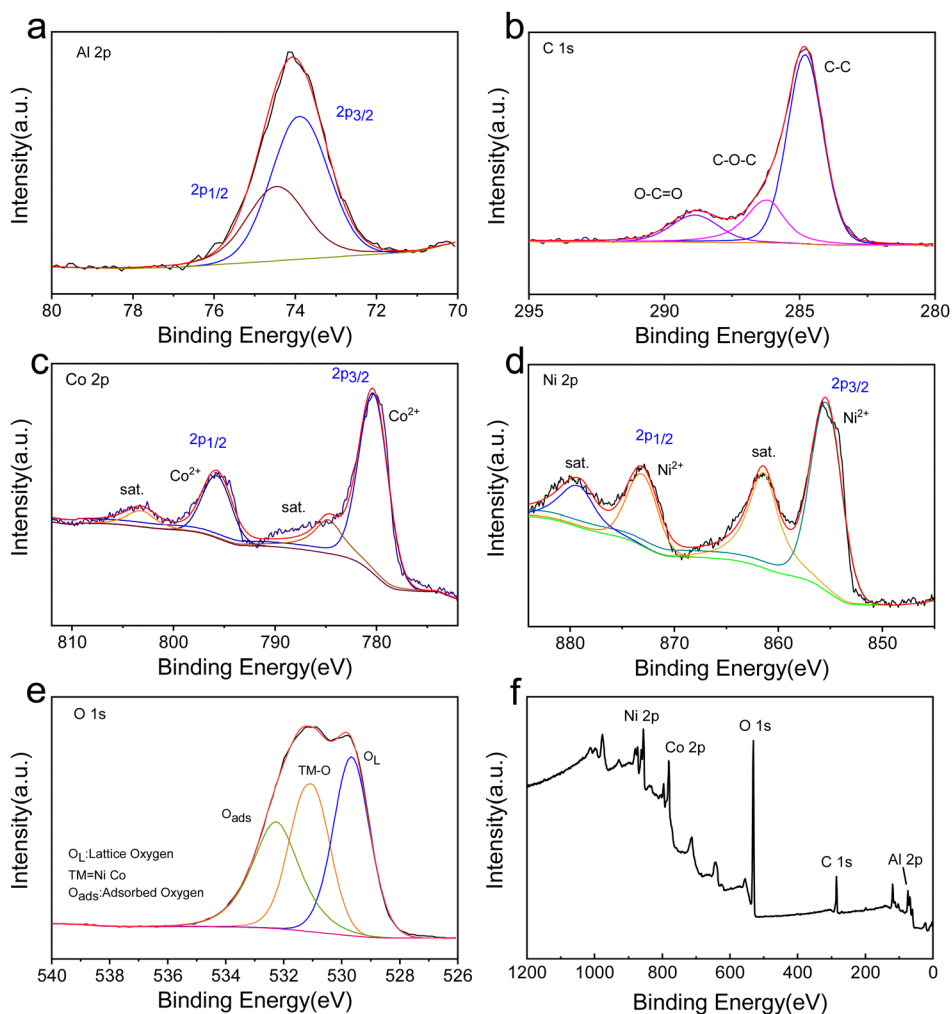

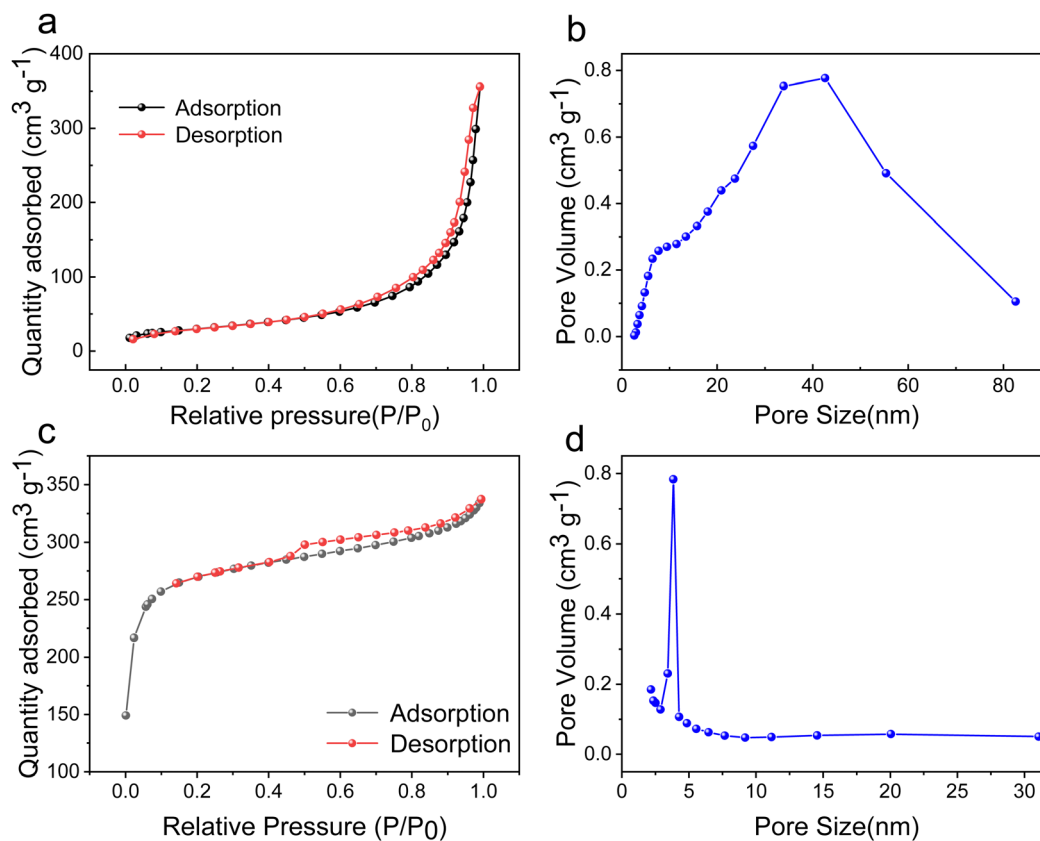**Fig. 2** High-resolution XPS spectra of (a) Al 2p, (b) C 1s, (b) Co 2p, (d) Ni 2p, and (e) O 1s. (f) Survey XPS spectra of $NiAl_2O_4/NiCo_2O_4$.

Fig. 3 (a) Nitrogen adsorption–desorption isothermal curves and (b) pore size distribution of $NiAl_2O_4/NiCo_2O_4$. (c) Nitrogen adsorption–desorption isothermal curves and (d) pore size distribution of the MOF.

The porous nature of $NiAl_2O_4/NiCo_2O_4$ can facilitate the ion transport in the electrolyte. As can be seen in Fig. 3c, a clear hysteresis regression line can be observed, forming a typical H1-type loop. Generally, H1-type hysteresis loops are found in ordered mesoporous materials. As shown in Fig. 3d, the pore size of the MOF mainly distributes in the range of 2–5 nm, which means that the MOF material is mesoporous. Comparing with the MOF material, the pore size of the MOF-derived material is much larger, which is due to the carbonization and decomposition of the organic ligands and structural changes during the annealing process. The large pores inside the MOF-derived structure provide more reactive active sites, which is conducive to the transport of ions.

Fig. 4 shows the SEM images and energy-dispersive X-ray spectra (EDS) of $NiAl_2O_4/NiCo_2O_4$. The SEM images show a loose irregular structure composed of inhomogeneous particles, which is due to the shrinkage and collapse of the part of the MOF structure. Because the organic ligands will carbonize and decompose during calcination, pre-calcination under a nitrogen atmosphere at 350 °C with subsequent calcination at 550 °C is needed to keep the original frame structure from completely collapsing. The porous structure promotes ion transport and charge transfer rates, which is beneficial for improving the electrochemical properties.[28] The pore size shown in SEM is about tens of nanometers, which is consistent with the results of nitrogen adsorption–desorption isotherms. The elemental mapping in

Fig. 4c–f shows the distribution of Ni, Co, Al, and O elements in $NiAl_2O_4/CoAl_2O_4$.

Fig. 4g–i show the TEM and HR-TEM images of $NiAl_2O_4/NiCo_2O_4$. The TEM images show that the synthesized particles are nearly spherical with a diameter of tens of nanometers. The HR-TEM images show that lattice fringes and amorphous structures can be observed simultaneously. As shown in Fig. 4i, the lattice fringe distances are determined to be 0.20 nm and 0.24 nm, which are related to the (311) and (400) planes of $NiAl_2O_4/NiCo_2O_4$, respectively.

3.2. Electrochemical tests

Fig. 5 shows the electrochemical properties of the $NiAl_2O_4/NiCo_2O_4$ material in a three-electrode system. Fig. 5a shows the cyclic voltammetric curves (CV) at different scanning speeds. It can be seen that there are obvious redox peaks, indicating that the electrode material is pseudocapacitive. With an increase in scanning speed, the CV area gradually increases while the reduction peak potential shifts negatively. However, the shape of the CV curves remained almost unchanged, indicating that the material has good electrochemical reversibility. Fig. 5b shows the GCD curves of the $NiAl_2O_4/NiCo_2O_4$ material measured at different current densities in the 0–0.48 V potential range. As the current density increases, the shape of the GCD curves did not change and a clear potential plateau appeared, indicating the pseudocapacitive properties and good stability.
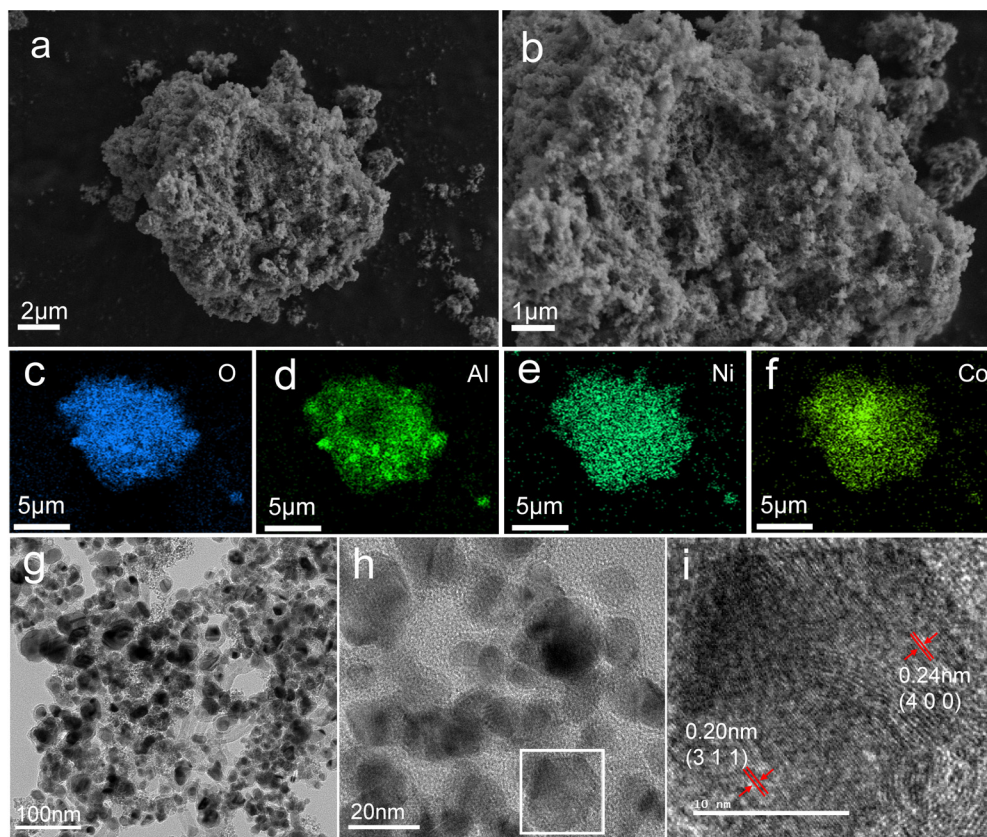
This journal is © the Owner Societies 2024

Phys. Chem. Chem. Phys., 2024, **26**, 6616–6626 | **6619**

Fig. 4 (a) and (b) SEM images with different magnifications. (c)–(f) EDS elemental mapping of O, Al, Ni, and Co. (g) TEM and (h) and (i) HR-TEM images with different magnifications of $NiAl_2O_4/NiCo_2O_4$.

The excellent specific capacitance may be attributed to the porous structure of the MOF, which provides many reaction sites and channels for free ion transport.

The mass specific capacitance (C, F g^{-1}) is calculated according to formula (1):[29]

$$C_m = \frac{I\Delta t}{m\Delta v} \quad (1)$$

where I is the discharge current (A), Δt is the discharge time (s), m is the mass of the active material (g), and Δv is the potential window (V).

At a current density of 1 A g^{-1}, the material has a specific capacitance of 2870.83 F g^{-1}. The excellent specific capacity is attributed to the large pore structure of the MOF, which provides many reactive sites and channels for free ion transport. Fig. 5c shows the rate performance at different current densities. As the current density increases, the discharge time decreases because the electrodes are charged and discharged too quickly, resulting in the electrolyte ions not completely entering the electrode material and an inadequate electrochemical reaction. To further explore the electrochemical mechanism of the $NiAl_2O_4/NiCo_2O_4$ material, electrochemical impedance spectroscopy (EIS) tests were performed in the range of 0.1 Hz–100 kHz. Fig. 5d shows the EIS spectra and fitted equivalent circuit diagrams of the $NiAl_2O_4/NiCo_2O_4$ material. The charge transfer resistance (R_{ct}) reflects the conductivity

between the active electrode material and the electrolyte, which can be calculated from the semicircular diameter of the high-frequency region of the EIS curve. The smaller the diameter, the higher the conductivity and ionic transfer rate. As can be seen, the semicircular arc in the high-frequency region is less pronounced, indicating a high ionic transfer rate between the material and the electrolyte. On the other hand, the straight line in the low-frequency region is related to the diffusion resistance (R_s). The greater the slope of the straight line, the more efficient ionic diffusion in the electrolyte.[30] The structure with large specific surface areas and abundant active sites helps to contact with the electrolyte ions.

Fig. 6 shows the cycling stability curve of the $NiAl_2O_4/NiCo_2O_4$ material at a current density of 10 A g^{-1}. The specific capacitance showed a trend of increasing and then decreasing and the retention reached 54.19% after 1000 cycles. With each cycle of charge and discharge, the electrolyte fully permeates the electrode material, increasing ion transport and capacitance in the first few cycles. Comparison with the literature in Table 1, the specific capacitance of $NiAl_2O_4/NiCo_2O_4$ was much higher while the cycling stability was lower. The poor cycle stability and Coulombic efficiency may be due to the following reasons: First, during charging and discharging, the electrode material might undergo repeated structural changes, such as volume expansion or contraction, leading to detachment of the electrode material. Second, some metals in the electrodes
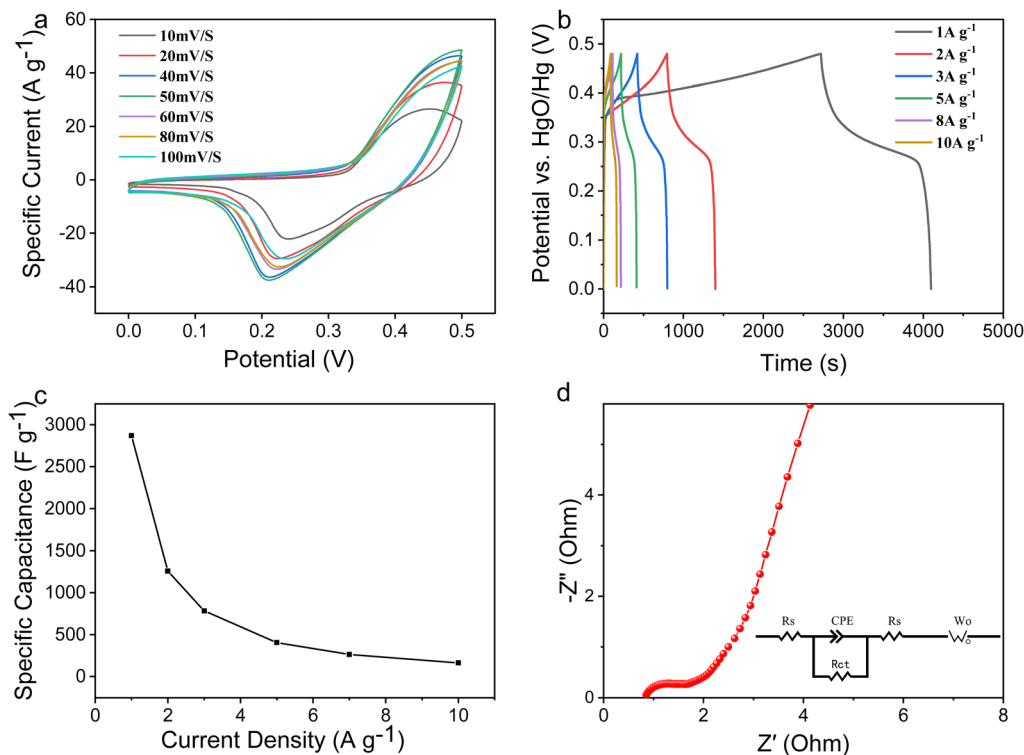
6620 | *Phys. Chem. Chem. Phys.*, 2024, **26**, 6616–6626

This journal is © the Owner Societies 2024

Fig. 5 (a) CV curves at different scanning speeds. (b) GCD curves at different current densities. (c) Specific capacitance at different current densities. (d) EIS curve in the frequency interval from 0.1 Hz to 100 kHz of $NiAl_2O_4/NiCo_2O_4$ in a three-electrode system.
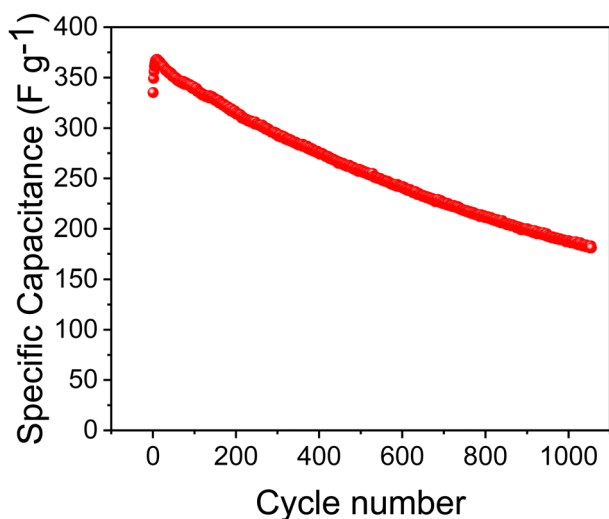

Fig. 6 Cycling stability of $NiAl_2O_4/NiCo_2O_4$ at 10 A g^{-1}.

might dissolve into the electrolyte. Finally, to save the measuring time (4100 s at 1 A g^{-1}), the cycling stability of the material was measured at a high current density of 10 A g^{-1}. A high current density will lead to a gradual loss of the electrode material and affects its cycling life.

The capacitance contribution can be qualitatively analyzed by the relationship between the current (i) and the scan rate (v) obtained from the CV curves:[31,32]

$$i = av^b \tag{2}$$

where a and b are constants. When plotted with $\log(i)$ against $\log(v)$, the value of b can be obtained from the slopes of the linear equations. Generally, the b value is between 0.5 (corresponding to a semi-infinite diffusion process) and 1 (corresponding to a capacitive process). As shown in Fig. 7a, the b value of $NiAl_2O_4/NiCo_2O_4$ was 0.52 in the scan rate range of 2–8 mV s^{-1}, indicating a typical capacitive behavior during the redox process. The capacitive contribution can be qualitatively calculated by the following equation:

$$i = k_1v + k_2v^{1/2} \tag{3}$$

where k_1 represents the capacitive effect and k_2 represents the diffusion process. In Fig. 7b, the area of the red shaded portion (k_1v) accounts for about 31% of the total area of the CV curve at a scan rate of 2 mV s^{-1}. Fig. 7c shows that the capacitive contribution gradually increases while the diffusive contribution decreases as the scan rate increases from 2 mV s^{-1} to 10 mV s^{-1}.

Fig. 8a shows the comparison of the CV curves of the $NiAl_2O_4/NiCo_2O_4$ material with the mono-metallic and bimetallic oxides at a scanning speed of 50 mV s^{-1}, in which a redox peak can be found in all the materials. The $NiAl_2O_4/NiCo_2O_4$ material has the largest CV curve area, indicating the best electrochemical properties. It can be further seen from Fig. 8b that the $NiAl_2O_4/NiCo_2O_4$ material has the longest discharge time, which makes it the best performing among

This journal is © the Owner Societies 2024

Phys. Chem. Chem. Phys., 2024, **26**, 6616–6626 | **6621**

Table 1 Comparison of the performance between this work and the literature

| Electrode material	Specific capacitance	Cycling efficiency	Ref.
Ov–Cu–Co$_3$O$_4$@C	927 C g^{-1} at 1 A g^{-1}	92.4% over 5000 cycles	10
NiZn-MOF	88.66 F g^{-1} at 1.1 A g^{-1}	90.05% over 2000 cycles	13
Cu/Cu$_x$O@NC	547 F g^{-1} at 1 A g^{-1}	91.81% over 10 000 cycles	14
CoZn-MOF	1205 F g^{-1} at 2 A g^{-1}	94.8% over 8000 cycles	15
(GNP)/MoS$_2$	311.14 F g^{-1} at 1 A g^{-1}	98.35% over 2000 cycles	18
NiAl$_2$O$_4$/NiCo$_2$O$_4$	2871 F g^{-1} at 1 A g^{-1}	54.19% over 1000 cycles	This work
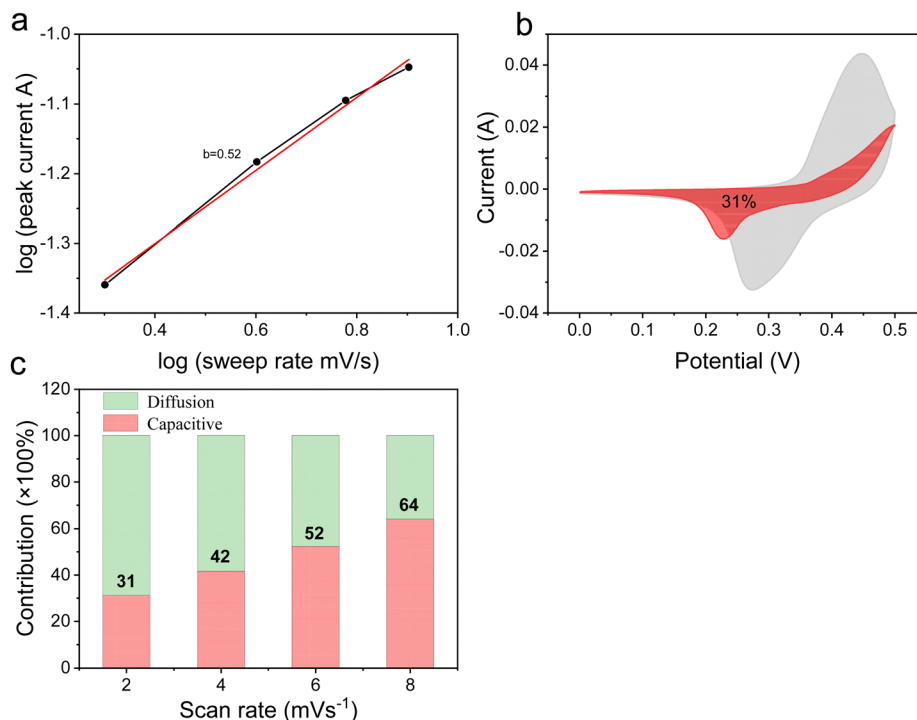
Fig. 7 (a) Relationship between the logarithm of the anode peak current and the scan rate, (b) capacitive contribution and the diffusive contribution at a scan rate of 2 mV s^{-1}, (c) capacitive and diffusive contribution ratios at different scan rates of NiAl$_2$O$_4$/NiCo$_2$O$_4$.

the four electrode materials at a current density of 1 A g^{-1}. The EIS spectra in Fig. 8c reveal that the NiAl$_2$O$_4$/NiCo$_2$O$_4$ material has the smallest semicircular radius in the high-frequency region, which means the smallest interfacial transfer resistance between the surface electrode and the electrolyte. In addition, the slope of the Nyquist curve of NiAl$_2$O$_4$/NiCo$_2$O$_4$ is significantly higher than that of other materials, which means it has better capacitive performance.[7]

In order to investigate the practical application of the NiAl$_2$O$_4$/NiCo$_2$O$_4$ electrode, the NiAl$_2$O$_4$/NiCo$_2$O$_4$//AC asymmetric supercapacitor was assembled with NiAl$_2$O$_4$/NiCo$_2$O$_4$ as the positive electrode and activated carbon (AC) as the negative electrode. Fig. 9a shows the CV curves of the AC electrode at different scanning speeds. The rectangular shape characteristic means a bilayer capacitance and a wide voltage of 1.0 V helps to widen the voltage window of the capacitor. Fig. 9b shows that the GCD curve of the AC electrode is close to a standard triangle, indicating that the material is a bilayer capacitor,[33] which is consistent with the results obtained from

the CV curves. Fig. 9c shows the CV curves of the positive electrode NiAl$_2$O$_4$/NiCo$_2$O$_4$ and the negative electrode AC measured at a scanning speed of 60 mV s^{-1}, which indicates that the working voltage window can reach 1.5 V or higher. Fig. 9d shows the CV curves of NiAl$_2$O$_4$/NiCo$_2$O$_4$//AC at different voltage windows with a scanning speed of 30 mV s^{-1}. It can be recognized that polarization can be seen on the CV curves when the working voltage exceeds 1.5 V. Therefore, the maximum voltage window of this energy storage device is 1.5 V, which is used in the subsequent testing of a two-electrode system.

To obtain the best performance of an asymmetric supercapacitor, the masses of the positive and negative electrodes are configured according to eqn (4):[34]

$$\frac{m^+}{m^-} = \frac{C^- \times \Delta V^-}{C^+ \times \Delta V^+} \qquad (4)$$

where m^+ and m^- are the masses of the electrode active substances (g), C^+ and C^- are the specific capacitances (F g^{-1}), and

6622 | *Phys. Chem. Chem. Phys.*, 2024, **26**, 6616–6626

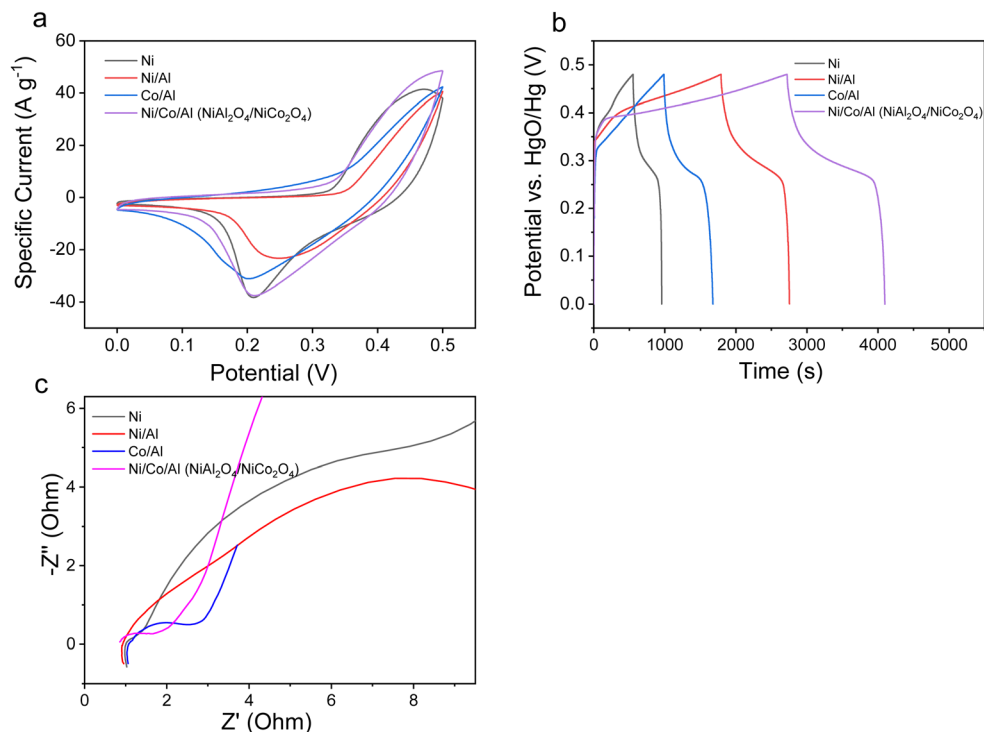This journal is © the Owner Societies 2024

Fig. 8 (a) cyclic voltammetric curve at 50 mV s^{-1}. (b) GCD curves at 1 A g^{-1}. (c) EIS spectra from 0.1 Hz to 100 kHz for mono-materials, bimetallic materials, and ternary materials.
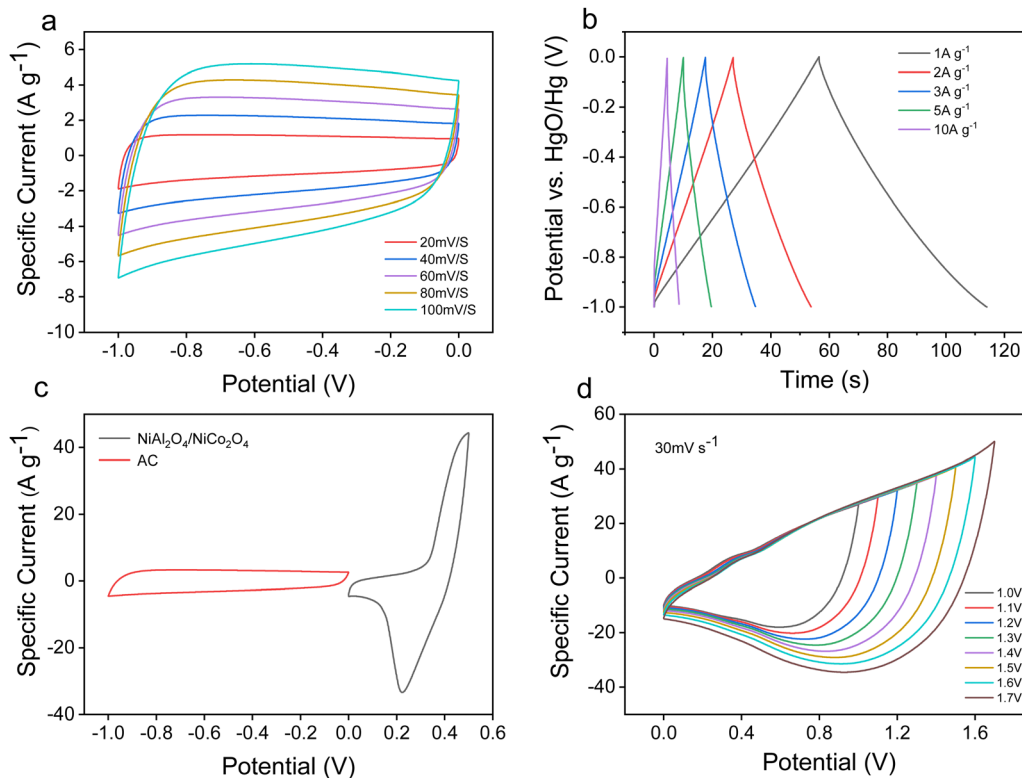

Fig. 9 (a) CV curves of AC electrodes at different scanning speeds. (b) GCD curves of AC electrodes at different current densities. (c) CV curves of negative AC and positive NiAl$_2$O$_4$/NiCo$_2$O$_4$ at a scanning speed of 60 mV s^{-1}. (d) CV curves of NiAl$_2$O$_4$/NiCo$_2$O$_4$//AC at different voltage windows with a scanning speed of 30 mV s^{-1}.

This journal is © the Owner Societies 2024

Phys. Chem. Chem. Phys., 2024, **26**, 6616–6626 | **6623**

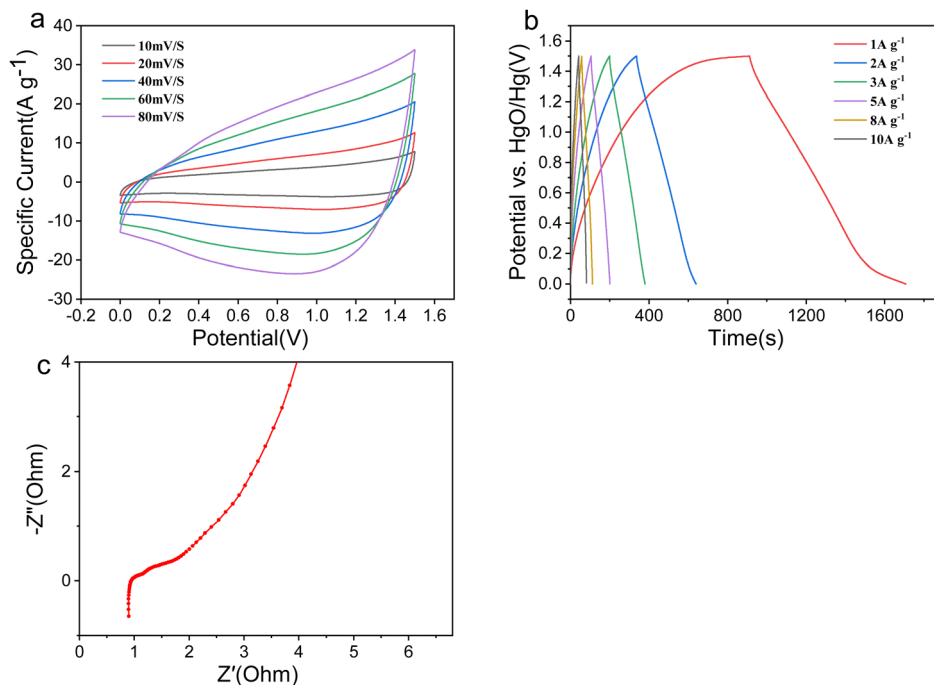**Fig. 10** NiAl$_2$O$_4$/NiCo$_2$O$_4$//AC asymmetric supercapacitors: (a) CV curves at different scanning speeds, (b) GCD curves at different current densities, and (c) EIS curves in the frequency range from 0.1 Hz to 100 kHz.

ΔV^+ and ΔV^- are the voltage windows (V) of the positive electrodes and negative electrodes, respectively.

Fig. 10a shows that the CV curves are rectangular-like shapes with redox peaks, indicating that the assembled asymmetric supercapacitor has both pseudocapacitance and double-layer performance. The triangle-like curves in Fig. 10b indicate that the device has pseudocapacitance and bilayer energy storage characteristics, which is consistent with the CV curves. The specific capacitance of NiAl$_2$O$_4$/NiCo$_2$O$_4$//AC is calculated to be 534.33 F g^{-1}. Fig. 10c shows the EIS curves of the NiAl$_2$O$_4$/NiCo$_2$O$_4$//AC device, in which the small radius indicates that the assembled asymmetric supercapacitor device has good conductivity.

The highest energy density (E) and power density (P) of NiAl$_2$O$_4$/NiCo$_2$O$_4$//AC can be calculated from eqn (5) and (6),[35] which are 166.98 W h kg^{-1} and 750.00 W kg^{-1}, respectively. Compared with the calcined Co$_3$O$_4$/NiO/Mn$_2$O$_3$ material[36] (the energy density is 65.7 W h kg^{-1}) and the hexagonal Al-MOF

material[4] (the specific capacitance is 342 F g^{-1} at 1 A g^{-1}) prepared by a solvothermal method, the device has superior energy storage performance.

$$E = \frac{CV^2}{2 \times 3.6} \qquad (5)$$

$$P = \frac{3600E}{t} \qquad (6)$$

where C is the specific capacitance (F g^{-1}), V is the voltage window (V), E is the energy density (W h kg^{-1}), and P is the power density (W kg^{-1}).

Fig. 11 shows the cycling stability of the ASC device of NiAl$_2$O$_4$/NiCo$_2$O$_4$//AC. The specific capacitance retention remains 72.8% after 2000 cycles at a current density of 4 A g^{-1}. This indicates that the ASC device exhibited good cyclic stability performance. By using two tandem NiAl$_2$O$_4$/NiCo$_2$O$_4$//AC devices, a low-power LED can be lighted, as shown in the inset.

4. Conclusions

The introduction of cobalt and aluminum increases the specific capacitance of NiO. The MOF structure maintained the original three-dimensional structure of the material, promoting the diffusion of ions and providing more active sites. MOF-derived NiAl$_2$O$_4$/NiCo$_2$O$_4$ electrode materials have a porous structure and a large specific surface area of 105 m^2 g^{-1}, as well as a great specific capacitance of 2870.83 F g^{-1} at a current density of 1 A g^{-1}. When assembled to an asymmetric super-capacitors with activated carbon, the device showed excellent electrochemical performance with an energy density of
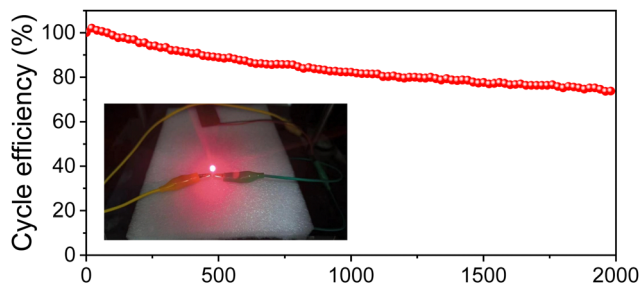

Fig. 11 Cycling stability of the ASC device NiAl$_2$O$_4$/NiCo$_2$O$_4$//AC and NiAl$_2$O$_4$/NiCo$_2$O$_4$//AC devices to light low-power LEDs.

6624 | *Phys. Chem. Chem. Phys.*, 2024, **26**, 6616–6626

This journal is © the Owner Societies 2024

166.98 W h kg^{-1} and a power density of 750.00 W kg^{-1}. This work provides a simple, effective, and promising preparation method for the application of supercapacitor materials.

Conflicts of interest

There are no conflicts to declare.

Acknowledgements

References

1 A. Abdisattar, M. Yeleuov, C. Daulbayev, K. Askaruly, A. Tolynbekov, A. Taurbekov and N. Prikhodko, Recent advances and challenges of current collectors for supercapacitors, *Electrochem. Commun.*, 2022, **142**, 107373.

2 S. H. Chen, L. Qiu and H. M. Cheng, Carbon-based fibers for advanced electrochemical energy storage devices, *Chem. Rev.*, 2020, **120**(5), 2811–2878.

3 Q. Dou and H. S. Park, Perspective on high-energy carbon-based supercapacitors, *Energy Environ. Mater.*, 2020, **3**(3), 286–305.

4 Q. C. Wang, B. Xiong and J. Q. Pan, Preparation of high porous carbon using Al-based MOFs and influence of dimethylformamide on morphological and electrochemical supercapacitor performances, *Int. J. Electrochem. Sci.*, 2022, **17**(220671), 2.

5 D. H. Hong, H. S. Shim, J. Ha and H. R. Moon, MOF-on-MOF architectures: applications in separation, catalysis, and sensing, *Bull. Korean Chem. Soc.*, 2021, **42**(7), 956–969.

6 I. Hussain, S. Iqbal, T. Hussain, W. L. Cheung, S. A. Khan, J. Zhou, M. Ahmad, S. A. Khan, C. Lamiel, M. Imran, A. AlFantazi and K. L. Zhang, Zn-Co-MOF on solution-free CuO nanowires for flexible hybrid energy storage devices, *Mater. Today Phys.*, 2022, **23**, 100655.

7 Y. Liu, A. Umar and X. Wu, Metal-organic framework derived porous cathode materials for hybrid zinc ion capacitor, *Rare Met.*, 2022, **41**(9), 2985–2991.

8 K. Wang, X. B. Zhong, Y. H. Zhang, P. T. Li, Y. Tan, Y. G. Zhang, Z. W. Zhang, J. Zhu, K. M. Shodievich, J. F. Liang and H. Wang, Economic synthesis of submicron brick-like Al-MOF with designed pore distribution for lithium-ion battery anodes with high initial Coulombic efficiency and cycle stability, *Dalton Trans.*, 2022, **51**(17), 6787–6794.

9 Y. X. Yang, K. K. Ge, S. U. Rehman and H. Bi, Nanocarbon-based electrode materials applied for supercapacitors, *Rare Met.*, 2022, **41**(12), 3957–3975.

10 S. Liu, L. Kang, J. Hu, E. Jung, J. Zhang, S. C. Jun and Y. Yamauchi, Unlocking the potential of oxygen-deficient copper-doped C$_3$O$_4$ nanocrystals confined in carbon as an advanced electrode for flexible solid-state supercapacitors, *ACS Energy Lett.*, 2021, **6**(9), 3011–3019.

11 Y. Yan, J. Lin, T. Xu, B. Liu, K. Huang, L. Qiao, S. Liu, J. Cao, S. C. Jun, Y. Yamauchi and J. Qi, Atomic-level platinum filling into Ni-vacancies of dual-deficient NiO for boosting electrocatalytic hydrogen evolution, *Adv. Energy Mater.*, 2022, **12**(24), 2200434.

12 S. Liu, L. Kang and S. C. Jun, Challenges and strategies toward cathode materials for rechargeable potassium-ion batteries, *Adv. Mater.*, 2021, **33**(47), 2004689.

13 J. Zeng, K. C. Devarayapalli, S. V. P. Vattikuti and J. Shim, Split-cell symmetric supercapacitor performance of bimetallic MOFs yolk-shell hierarchical microstructure, *Mater. Lett.*, 2022, **309**, 131305.

14 Z. Abbas, N. Hussain, I. Ahmed and S. M. Mobin, Cu-Metal organic framework derived multilevel hierarchy (Cu/Cux-O@NC) as a bifunctional electrode for high-performance supercapacitors and oxygen evolution reaction, *Inorg. Chem.*, 2023, **62**(23), 8835–8845.

15 S. Salehi, M. H. Ehsani and M. Aghazadeh, Novel electrodeposition of bud-like cobalt/zinc metal-organic-framework onto nickel foam as a high-performance binder-free electrode material for supercapacitor applications, *Mater. Lett.*, 2022, **319**, 132282.

16 K. Nabeela, R. Deka, Z. Abbas, P. Kumar, M. Saraf and S. M. Mobin, Weak Bonds, Strong Effects: Enhancing the Separation Performance of UiO-66 toward chlorobenzenes via halogen bonding, *Cryst. Growth Des.*, 2023, **23**(5), 3057–3078.

17 S. N. Ansari, M. Saraf, Z. Abbas and S. M. Mobin, Heterostructures of MXenes and transition metal oxides for supercapacitors: an overview, *Nanoscale*, 2023, **15**, 13546–13560.

18 Z. Abbas, P. Tiwari, V. Kumar and S. M. Mobin, Gelatin-assisted co-exfoliation of graphene nanoplatelets/MoS$_2$ for high-performance supercapacitors, *Sustainable Energy Fuels*, 2022, **6**(16), 3872–3883.

19 Y. F. Ren, Z. L. He, H. Z. Zhao and T. Zhu, Fabrication of MOF-derived mixed metal oxides with carbon residues for pseudocapacitors with long cycle life, *Rare Met.*, 2022, **41**(3), 830–835.

20 L. J. Yan, L. Y. Niu, C. Shen, Z. K. Zhang, J. H. Lin, F. Y. Shen, Y. Y. Gong, C. Li, X. J. Liu and S. Q. Xu, Modulating the electronic structure and pseudocapacitance of delta-MnO$_2$ through transition metal M (M = Fe, Co and Ni) doping, *Electrochim. Acta*, 2019, **306**, 529–540.

21 C. W. Gao, P. X. Wang, Z. Y. Wang, S. K. Kaer, Y. F. Zhang and Y. Z. Yue, The disordering-enhanced performances of the Al-MOF/graphene composite anodes for lithium ion batteries, *Nano Energy*, 2019, **65**, 104032.

22 Y. Z. Wang, Y. X. Liu, H. Q. Wang, W. Liu, Y. Li, J. F. Zhang, H. Hou and J. L. Yang, Ultrathin NiCo-MOF nanosheets for high-performance supercapacitor electrodes, *ACS Appl. Energy Mater.*, 2019, **2**(3), 2063–2071.

23 S. Chinnapaiyan, H. T. Das, S. M. Chen, M. Govindasamy, R. A. Alshgari, C. H. Fan and C. H. Huang, CoAl$_2$O$_4$ nanoparticles modified carbon nanofibers as high-efficiency

bifunctional electrocatalyst: an efficient electrochemical aqueous asymmetric supercapacitors and non-enzymatic electrochemical sensors, *J. Alloys Compd.*, 2023, **931**, 167553.

24 F. Lv, W. Y. Zhang, L. He, X. Bai, Y. Song and Y. Zhao, 3D porous flower-like $CoAl_2O_4$ to boost the photocatalytic CO_2 reduction reaction, *J. Mater. Chem. A*, 2023, **11**(6), 2826–2835.

25 D. Y. Gao, R. N. Liu, D. D. Han, P. C. Xu, P. Wang and Y. Wei, Constructing Ni-Co PBA derived 3D/1D/2D NiO/$NiCo_2O_4$/NiMn-LDH hierarchical heterostructures for ultra-high rate capability in hybrid supercapacitors, *J. Mater. Chem. A*, 2023, **11**(17), 9546–9554.

26 M. Khot, R. S. Shaik, W. Touseef and A. Kiani, Binder-free NiO/CuO hybrid structure via ULPING (ultra-short laser pulse for in-situ nanostructure generation) technique for supercapacitor electrode, *Sci. Rep.*, 2023, **13**(1), 6975.

27 E. Regulska, J. Breczko, A. Basa, B. Szydlowska, K. Kakareko, A. Rydzewska-Rosolowska and T. Hryszko, Graphene-quantum-dots-decorated $NiAl_2O_4$ nanostructure as super-capacitor and electrocatalyst in biosensing, *Mater. Today Commun.*, 2022, **33**, 104116.

28 G. Z. Zhao, L. Han, K. Ning, G. Zhu, J. Yang and H. Y. Wang, O doped Tremella-shaped porous carbon for zinc-ion hybrid capacitors with long life and enhanced energy density, *Mater. Lett.*, 2022, **329**, 133180.

29 S. Seenivasan, K. I. Shim, C. Lim, T. Kavinkumar, A. T. Sivagurunathan, J. W. Han and D. Kim, Boosting pseudocapacitive behavior of supercapattery electrodes by incorporating a Schottky junction for ultrahigh energy density, *Nano-Micro Lett.*, 2023, **15**(1), 62.

30 A. Agrawal, A. Gaur and A. Kumar, Fabrication of Phyllanthus emblica leaves derived high-performance activated carbon-based symmetric supercapacitor with excellent cyclic stability, *J. Energy Storage*, 2023, **66**, 107395.

31 D. Chao, P. Liang, Z. Chen, L. Bai, H. Shen, X. Liu, X. Xia, Y. Zhao, S. V. Savilov, J. Lin and Z. X. Shen, Pseudocapacitive Na-ion storage boosts high rate and areal capacity of self-branched 2d layered metal chalcogenide nanoarrays, *ACS Nano*, 2016, **10**(11), 10211–10219.

32 X. Pu, D. Zhao, C. Fu, Z. Chen, S. Cao, C. Wang and Y. Cao, Understanding and calibration of charge storage mechanism in cyclic voltammetry curves, *Angew. Chem., Int. Ed.*, 2021, **60**(39), 21310–21318.

33 Y. Sun, S. Xue, J. Sun, X. Li, Y. Ou, B. Zhu and M. Demir, Silk-derived nitrogen-doped porous carbon electrodes with enhanced ionic conductivity for high-performance super-capacitors, *J. Colloid Interface Sci.*, 2023, **645**, 297–305.

34 B. N. V. Krishna, O. R. Ankinapalli, A. R. Reddy and J. S. Yu, Facile one-step hydrothermal route to MSe/Mo_3Se_4 (M: Zn, Mn, and Ni)-based electrode materials for ultralong-life hybrid supercapacitors, *Mater. Sci. Technol.*, 2023, **156**, 230–240.

35 X. L. Su, J. R. Chen, G. P. Zheng, J. H. Yang, X. X. Guan, P. Liu and X. C. Zheng, Three-dimensional porous activated carbon derived from loofah sponge biomass for supercapacitor applications, *Appl. Surf. Sci.*, 2018, **436**, 327–336.

36 S. T. Li, Y. A. Duan, Y. Teng, N. Fan and Y. Q. Huo, MOF-derived tremelliform Co_3O_4/NiO/Mn_2O_3 with excellent capacitive performance, *Appl. Surf. Sci.*, 2019, **478**, 247–254.

6626 | *Phys. Chem. Chem. Phys.*, 2024, **26**, 6616–6626

This journal is © the Owner Societies 2024